Received: 1 March 2019 | Revised: 30 August 2019 | Accepted: 27 September 2019 | Published on: 2 December 2019

DOI: 10.1002/qj.3672

RESEARCH ARTICLE

Quarterly Journal of the Royal Meteorological Society RMetS

# Mesoscale precipitation systems and their role in the rapid development of a monsoon depression over the Bay of Bengal

Hatsuki Fujinami | Hidetaka Hirata | Masaya Kato | Kazuhisa Tsuboki

Institute for Space-Earth Environmental Research, Nagoya University, Nagoya, Japan

**Correspondence**
H Fujinami, Institute for Space-Earth Environmental Research, Nagoya University, Furo-cho, Chikusa-ku, Nagoya 464-8601, Japan.
Email: hatsuki@nagoya-u.jp

**Present address**
Hidetaka Hirata, Department of Environmental Systems, Faculty of Geo-Environmental Sciences, Rissho University, Kumagaya, Japan

**Funding information**
Japan Society for the Promotion of Science, KAKENHI Grants JP 18KK0098, KAKENHI Grants JP 26220202, KAKENHI Grants JP 26400465

## Abstract

The structure of mesoscale precipitation within monsoon depressions is still not as well-known as the synoptic-scale composite cloud and precipitation structure. Here, using observational data from multi-satellite sensors and a cloud-resolving regional model, we investigate the three-dimensional structure of mesoscale precipitation systems in the different stages of the life cycle of a monsoon depression. Effects of latent heating from the precipitation systems and the Bay of Bengal (BoB) on the development of the monsoon depression are also evaluated in sensitivity experiments with the model. A typical monsoon depression developed on 17 August 2016 over the BoB. In the rapid development phase, satellite observations reveal mesoscale convective systems with deep convective precipitation cells and stratiform precipitation near the head of the BoB. Extremely deep and intense convective cells appear along a ring-like rain band when a closed cyclonic circulation becomes obvious around the northernmost part of the BoB. The deep convection appears frequently, particularly along the western-to-southwestern side of the low, a convergence-prone area between northerlies with air masses of large convective available potential energy (CAPE) that makes up the western–southwestern part of the closed cyclonic circulation, and strong monsoon westerlies with relatively stable air masses to the south of the low. Sensitivity experiments reveal that both cloud/precipitation processes and evaporation from the BoB are essential for the rapid development of the monsoon depression over the BoB. Evaporation from the BoB adds a large amount of moisture to the atmospheric boundary layer near the low. Southwesterlies and southerlies on the eastern side of the low draw in warm, humid boundary-layer air to the closed cyclonic circulation, which maintains a large-CAPE environment in the low and enhances deep convection. A possible positive feedback process including moist convection that leads to the rapid intensification of monsoon depressions over the BoB is discussed.

**KEYWORDS**

cloud-resolving regional model, latent heating, mesoscale precipitation system, monsoon depression, spaceborne precipitation and cloud radar

  

# 1 | INTRODUCTION

Synoptic-scale monsoon low-pressure systems (LPSs) contribute a large fraction of total summer monsoon rainfall (Hurley and Boos, 2015; Praveen *et al.*, 2015), especially over land in South Asia and Australia (Yoon and Chen, 2005; Krishnamurthy and Ajayamohan, 2010; Berry *et al.*, 2012). Extreme precipitation and catastrophic floods in South Asia are often associated with LPSs (Houze *et al.*, 2011; Webster *et al.*, 2011; Joseph *et al.*, 2015; Bohlinger *et al.*, 2017). In addition, LPSs play a role in the transport of water vapour toward high mountain areas such as the Himalayas and the Tibetan Plateau, affecting precipitation processes in these regions (Lang and Barros, 2002; Ueno *et al.*, 2008; Dong *et al.*, 2016; 2017; 2018). Thus, LPSs play an important role in forming the hydroclimate around their tracks and surrounding areas.

The study of LPSs around India has the longest history among all monsoon areas. LPSs around India are categorized into lows, depressions, deep depressions and cyclonic storms based on their intensity in terms of surface wind speed (Saha *et al.*, 1981; Hurley and Boos, 2015). Monsoon depressions have surface wind speeds of 8.5–13.5 $m \cdot s^{-1}$. On average, about 15–35% of LPSs during June–September are categorized as monsoon depressions (Hurley and Boos, 2015; Praveen *et al.*, 2015; Hunt and Fletcher, 2019). Typically, LPSs including monsoon depressions form over the head of the Bay of Bengal (BoB) and move northwestward over the Indian subcontinent, with a life cycle of 3–6 days and a horizontal scale of ∼1,000–2,000 km (Godbole, 1977; Sikka, 1977). The genesis location and track of LPSs were recently reconfirmed by tracking methods using state-of-the-art atmospheric reanalysis data (Krishnamurthy and Ajayamohan, 2010; Hatsuzuka *et al.*, 2014; Hurley and Boos, 2015; Hunt *et al.*, 2016a).

The structure of Indian monsoon depressions is characterized by a vertical tilt to the west and south, a warm-over-cold temperature anomaly in the centre of the depression, peak horizontal winds at 700–800 hPa with cyclonic winds extending from the surface to the upper troposphere, and precipitation/cloud maxima in the west–southwest of the depression (Godbole, 1977; Krishnamurthy and Ajayamohan, 2010). Recently, more detailed three-dimensional composite structures of monsoon depressions have been presented, based on more than 100 cases, using high-spatial-resolution atmospheric reanalysis and satellite datasets (Hurley and Boos, 2015; Hunt *et al.*, 2016a). These composite structures have revealed the robust features of monsoon depressions including the known features mentioned above and, in addition, a deep column of high potential vorticity (PV) extending from the surface to the upper troposphere with PV maximum at around 500 hPa and a weaker maximum around 700–850 hPa. The low-level horizontal wind maximum and relevant relative vorticity maximum are associated with the maximum around 700–850 hPa, whereas a warm core around 350 hPa, which is mainly due to latent heating from condensation, causes the PV maximum around 500 hPa (Hunt *et al.*, 2016a), indicating the dominance of diabatic processes (e.g. latent heating) in the growth of monsoon depressions. Murthy and Boos (2019) found that both deep convective and stratiform heating produce PV maxima around 500 hPa in tropical depressions. Previous studies have proposed moist baroclinic instability as a possible cause of depression growth (e.g. Moorthi and Arakawa, 1985; Krishnamurti *et al.*, 2013). Cohen and Boos (2016) argued against this theory, based on a comparison of the vertical structure of monsoon depressions, hurricanes and diabatic Rossby waves, and indicated that the growth of monsoon depressions is more closely related to tropical depression spin-up than to moist baroclinic instability. However, a common finding of previous studies is that diabatic heating from moist convection plays a key role in the development of monsoon depressions.

Recent studies have reported a favourable environment for the genesis of LPSs around South Asia (Yanase *et al.*, 2012; Tsuboi and Takemi, 2014; Ditchek *et al.*, 2016; Hatsuzuka and Fujinami, 2017; Samanta *et al.*, 2018). Humid and convectively unstable environments with high cyclonic vorticity and high sea-surface temperature (SST) favour genesis over the northwestern BoB despite relatively strong vertical wind shear due to the vertical structure of a large-scale Asian monsoon circulation. The environment is strongly modulated by intraseasonal oscillations such as the boreal summer intraseasonal oscillation (BSISO: e.g. Wang *et al.*, 2006; Kikuchi *et al.*, 2012) and quasi-biweekly oscillation (QBW: e.g. Chattergee and Goswami, 2004; Fujinami *et al.*, 2014), clustering the genesis points and tracks of LPSs between active and break phases of intraseasonal oscillations (Goswami *et al.*, 2003; Krishnamurthy and Ajayamohan, 2010; Yanase *et al.*, 2012; Hatsuzuka and Fujinami, 2017).

The composite three-dimensional structure of precipitation has also been investigated using Tropical Rainfall Measuring Mission (TRMM)–Precipitation Radar (PR) data and the CloudSat–Cloud Profiling Radar (CPR) (Stano *et al.*, 2002; Hunt *et al.*, 2016b). These studies showed composite "synoptic-scale" features of hydrometeors in monsoon depressions. Intense convection occurs in the south–southwest of monsoon depressions, with significant precipitation for hundreds of kilometres outside the centre and well above the mid-troposphere.

However, the composite analysis obscures mesoscale features such as rain bands and convective systems in monsoon depressions. In addition, the mesoscale hydrometeor structure might change in different stages of the life cycle. Therefore, in this study we investigate mesoscale precipitation and cloud features inside a synoptic-scale monsoon depression using multi-satellite sensors. We focus on the monsoon

depression that occurred over the head of the BoB on 17 August 2016. It persisted as a monsoon depression until 20 August (e.g. India Meteorological Department cyclone eAtlas; http://www.rmcchennaieatlas.tn.nic.in). Fortunately, several overpasses of the Global Precipitation Measurement (GPM) satellite with a spaceborne precipitation radar captured the evolution of the monsoon depression from the development phase to the decaying phase after landfall. CloudSat with a cloud-profiling radar and a geostationary meteorological satellite also observed the depression during this period. Thus, we can capture the three-dimensional features of mesoscale precipitation/cloud systems of the monsoon depression using multi-satellite sensors.

We also investigate the development of the monsoon depression and the spatio-temporal structure of mesoscale precipitation systems using a cloud-resolving regional model and observational data. Previous studies have not investigated mesoscale precipitation/convection systems of monsoon depressions using cloud-resolving models. Some previous studies have used the Weather Research and Forecasting (WRF) model to investigate the relationship between land surface feedback and landfalling monsoon depressions (Chang *et al.*, 2009; Baisya *et al.*, 2017) and between cloud condensation nuclei and the intensity of monsoon depressions through sensitivity experiments (Krishnamurti *et al.*, 2013). As demonstrated below, monsoon depressions do involve mesoscale convective systems (MCSs) with deep convective cells and precipitating stratiform cloud regions. Thus, non-hydrostatic and compressible cloud-resolving models are required to better represent and understand MCSs within monsoon depressions and the development of monsoon depressions.

Sensitivity experiments are also carried out to evaluate the effects of latent heating due to condensation and evaporation from the BoB on the development of the monsoon depression, using the numerical model. We do not deal with the detailed processes involved in the genesis of the monsoon depression in the present article.

## 2 | DATA AND MODEL USED

### 2.1 | Data

We used precipitation data from the GPM Core Observatory that carries the first spaceborne dual-frequency phased array precipitation radar (DPR), operating at Ku and Ka bands (13 and 35 GHz, respectively) and a conical-scanning multichannel (10–183 GHz) Global precipitation measurement Microwave Imager (GMI: Hou *et al.*, 2014). The DPR can observe the three-dimensional structure of precipitation. The DPR L2 data version 04A (Iguchi *et al.*, 2015) were used in this study. The horizontal resolution of DPR is 5.0 km at nadir; the vertical resolution is 250 m. The minimum detectable

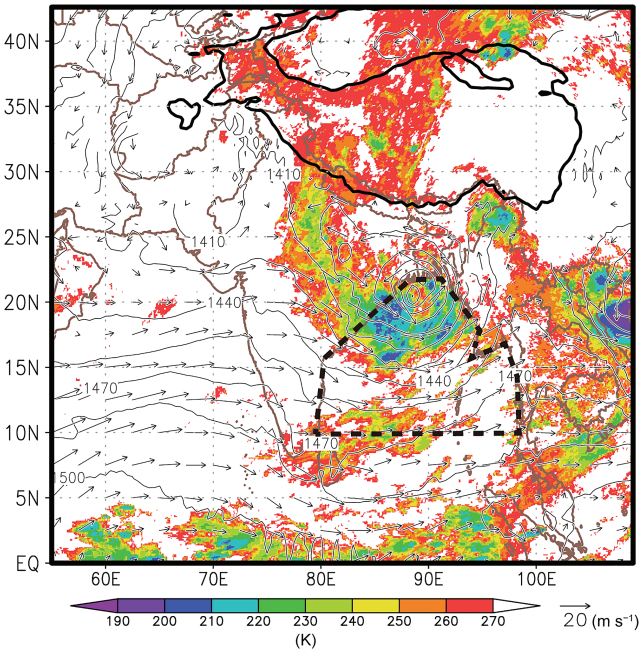


**FIGURE 1** Distribution of infrared brightness temperature (shading, K) from GridSat data, 850 hPa geopotential height (contours, gpm) and 850 hPa wind field (vectors) from the NCEP CFSv2 at 0000 UTC 17 August 2016. The contour interval for geopotential height is 15 gpm. The area shown (0°N–42.6°N, 55°E–109°E) corresponds to the model domain for the numerical simulation using CReSS. The area enclosed by the thick dashed line indicates the area for the sensitivity experiment excluding latent-heat flux from the Bay of Bengal. See details of the numerical simulation in the text. The thick solid line denotes the 3,000 m topographic contour [Colour figure can be viewed at wileyonlinelibrary.com].

rainfall rate is about 0.2 mm·h$^{-1}$ and the swath width is about 125 km. The GMI with a swath of 885 km can observe the horizontal structure of precipitation over a wider area than the DPR. GMI L2 data version 04a were used.

CloudSat Cloud Profiling Radar (CPR) data were used to investigate the vertical structure of cloud in the monsoon depression. The radar measures at nadir only and therefore the output swaths have effectively zero width. Radar reflectivity data from the 2B-GEOPROF R04 product were used. The along-track resolution is 1.7 km and the vertical resolution is 250 m. We also used Gridded Satellite (GridSat) B1 data to show the cloud distribution over the whole analysis domain (Figure 1). GridSat B1 data are a high-quality Climate Data Record (CDR) of global infrared measurements from geostationary satellites, based on the International Satellite Cloud Climatology Project (ISCCP) B1 dataset (Knapp *et al.*, 2011). The data are on a 0.07° latitude × 0.07° longitude grid with a 3-hourly time interval.

The observation frequency of the GPM and CloudSat satellites for a single location is low because of the orbit, and the observation width is limited. Therefore, successive observations of precipitation/clouds in a single synoptic-scale disturbance are unlikely. However, these satellites do provide

detailed three-dimensional structures of precipitation/clouds when data are available. In contrast, GridSat data provide continuous brightness temperature data for a broad area from the infrared channel of geostationary satellites. The complimentary use of multiple satellites can thus reveal the mesoscale features of precipitation/clouds in monsoon depressions.

We used the National Centers for Environmental Prediction (NCEP) Climate Forecast System version 2 (CFSv2) data on a 0.5° × 0.5° grid to investigate the atmospheric circulation related to the monsoon depression (Saha *et al.*, 2010).

## 2.2 | Model and experimental design

We used the Cloud Resolving Storm Simulator (CReSS: Tsuboki and Sakakibara, 2002; 2007; Tsuboki, 2008), which is a non-hydrostatic and compressible model, to simulate the monsoon depression. CReSS has been used to examine various low-pressure systems such as typhoons, cyclones and midlatitude cyclones, and their associated mesoscale cloud/precipitation systems (e.g. Akter and Tsuboki, 2012; Hirata *et al.*, 2015; 2016; Tsuboki *et al.*, 2015). A bulk parametrization for cold rain (Murakami, 1990; Ikawa and Saito, 1991; Murakami *et al.*, 1994) was applied to cloud microphysical processes. The microphysical schemes used in the model included both prognostic equations for the mixing ratio of water vapour, cloud water, cloud ice, rain, snow and graupel, and for the number concentrations of cloud ice, snow and graupel. A 1.5-order turbulent kinetic energy closure scheme (Deardorff, 1980) was used for subgrid-scale turbulence processes. The model domain was South Asia and its surroundings, including the Himalayas and the Tibetan Plateau (55°–109°E, 0°–42.6°N; the whole domain of Figure 1) and the horizontal grid resolution was 0.05° longitude × 0.05° latitude. The atmospheric vertical coordinate was a terrain-following coordinate, and 45 vertical layers were included with the top level at a height of 22.5 km. The time step for terms related to sound waves was 2.0 s, and for other terms was 6.0 s. We selected 1200 UTC on 14 August 2016 as the initial time and the integration period was 7 days. The initial and lateral boundary conditions for CReSS were derived from the NCEP CFSv2 data with a time resolution of 6 h and a spatial resolution of 0.5° longitude × 0.5° latitude. We used the daily National Oceanic Atmospheric Administration (NOAA) optimal interpolation (OI) sea-surface temperature (SST) with a spatial resolution of 0.25° × 0.25° at the initial time of the simulation. The initial conditions were specified throughout all grid cells of the CReSS domain, while during the rest of the integration only lateral boundary conditions were applied. With this configuration of CReSS, we performed three different experiments: a control experiment (CNTL run) and two sensitivity experiments comprising the NCP (i.e. no cloud microphysical processes) run and the NEV (i.e. no evaporation from the BoB) run to evaluate the effect of latent heating on the development of the monsoon depression. In the NCP run, cloud microphysical processes are switched off during the simulation and therefore condensation does not occur in the simulation domain; thus, it behaves as a dry model without considering condensation or precipitation. In contrast, the NEV run only switches off evaporation from the BoB (i.e. the area enclosed by the thick dashed line in Figure 1) to evaluate the effect of latent-heat flux (i.e. evaporation) from the BoB, although cloud microphysical processes are included in the experiment, as in the CNTL run.

# 3 | RESULTS

## 3.1 | Hydrometeor structure

In this section, we investigate the hydrometeor structure of the monsoon depression on both the synoptic and meso-scales during its life cycle. Figure 1 shows the monsoon depression at 0000 UTC 17 August 2016 when it reached minimum central pressure over the head of the BoB during its life cycle (Figure 2). Deep convection (<200 K) that reaches above 15 km develops south of its centre, especially in the southwest, while convective activity is suppressed from the north to east of the centre, showing a synoptic-scale cloud distribution that is typical of monsoon depressions (Godbole, 1977; Sikka, 1977; Stano *et al.*, 2002; Hunt *et al.*, 2016b; Fujinami *et al.*, 2017). Active convection extends from the southwestern part of the monsoon depression to the western Tibetan Plateau across the western Himalayas, corresponding to the convergence zone between the prevailing monsoon westerlies and the easterlies in the northern part of the depression in the lower troposphere.

Figure 2 shows time series of the central pressure of the monsoon depression from the CFSv2 data and the CNTL run by CReSS from 0000 UTC 16 August to 1200 UTC 21 August. The CFSv2 data reveal that the central pressure decreases rapidly from 0000 UTC 16 August and reaches a minimum at 0000 UTC 17 August, followed by a gradual increase. Figure 3 shows the time sequence of the monsoon depression and its hydrometeors from 15 to 18 August. Dates and times for the figures correspond to the four overpasses of the GPM observatory over the monsoon depression (Figure 3e–h). The observation time for infrared brightness temperature from GridSat (Figure 3a–d) corresponds closely to that from the GPM observations. At 0000 UTC 16 August (Figure 3a), a day before the low reached monsoon depression intensity, the head of the BoB is largely covered by clouds with a few contiguous cold cloud areas. Active convection is observed in the cloud area, accompanied by high precipitation (>20 mm·h$^{-1}$) (Figure 3e). A small vortex with a closed contour appears centred on 20°N, 90°E (Figure 3a) and is

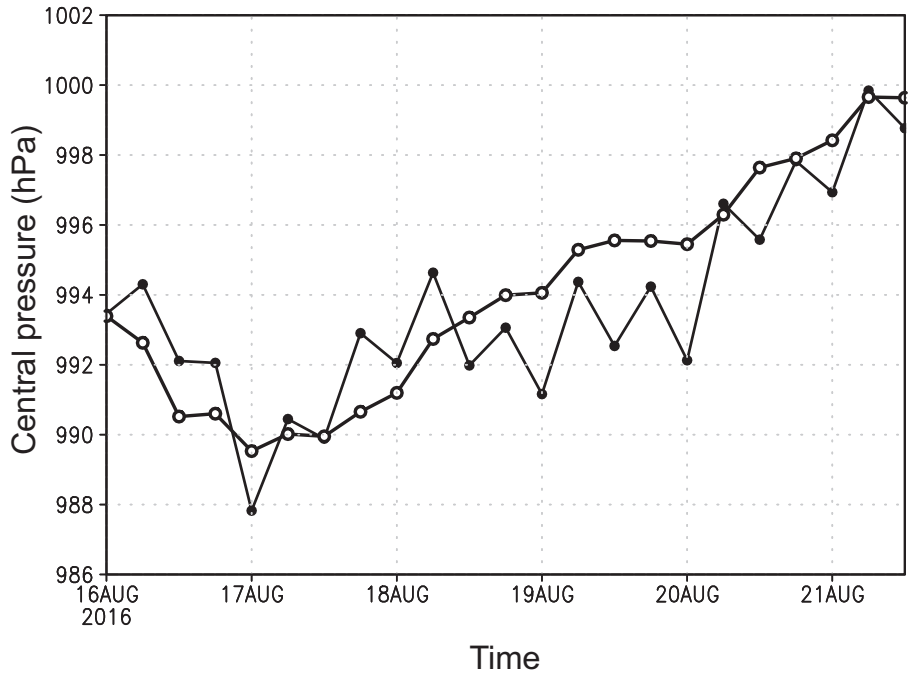


**FIGURE 2** Time series of the central pressure of a monsoon depression based on CFSv2 data (solid line with closed circles) and the CReSS CNTL run (solid line with open circles)

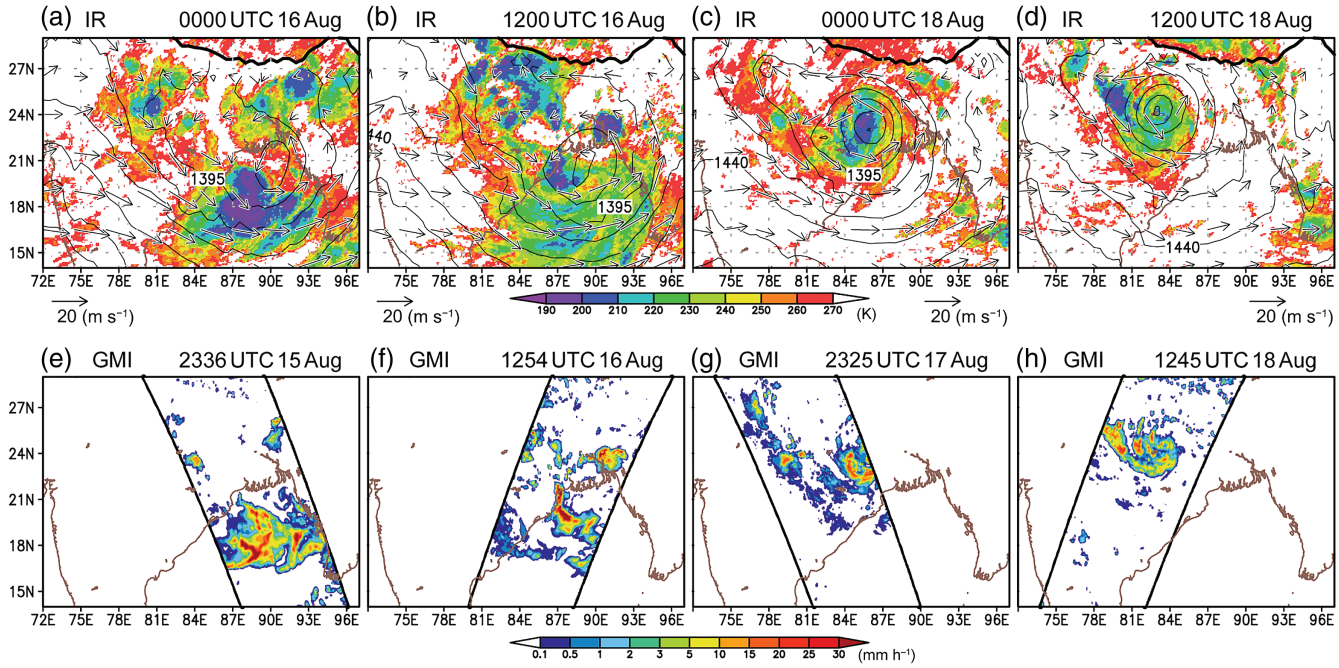


**FIGURE 3** Distribution of infrared brightness temperature (shading, K) from GridSat data and 850 hPa geopotential height (contours, gpm) and wind field (vectors) from the NCEP CFSv2 at (a) 0000 UTC 16 August, (b) 1200 UTC 16 August, (c) 0000 UTC 18 August, and (d) 1200 UTC 18 August in 2016. The contour interval for geopotential height is 15 gpm. Also shown is precipitation (mm·h$^{-1}$) derived from the GMI at (e) 2336 UTC 15 August, (f) 1254 UTC 16 August, (g) 2325 UTC 17 August and (h) 1245 UTC 18 August. The area enclosed by thick solid lines represents the GMI swath [Colour figure can be viewed at wileyonlinelibrary.com].

observed from 0000 UTC 15 August over the head of the BoB (not shown).

The vortex structure of the low becomes obvious at the head of the BoB from 1200 UTC 16 August (Figure 3b). The BoB is largely covered by clouds, but active convection is confined along the closed contour of the vortex (i.e. the 1,380 gpm contour in Figure 3b) away from its centre. This feature is more remarkable in the precipitation distributions from the GMI (Figure 3f); high precipitation occurs in a ring-like rain band at a radial distance of ~200–300 km from the centre of

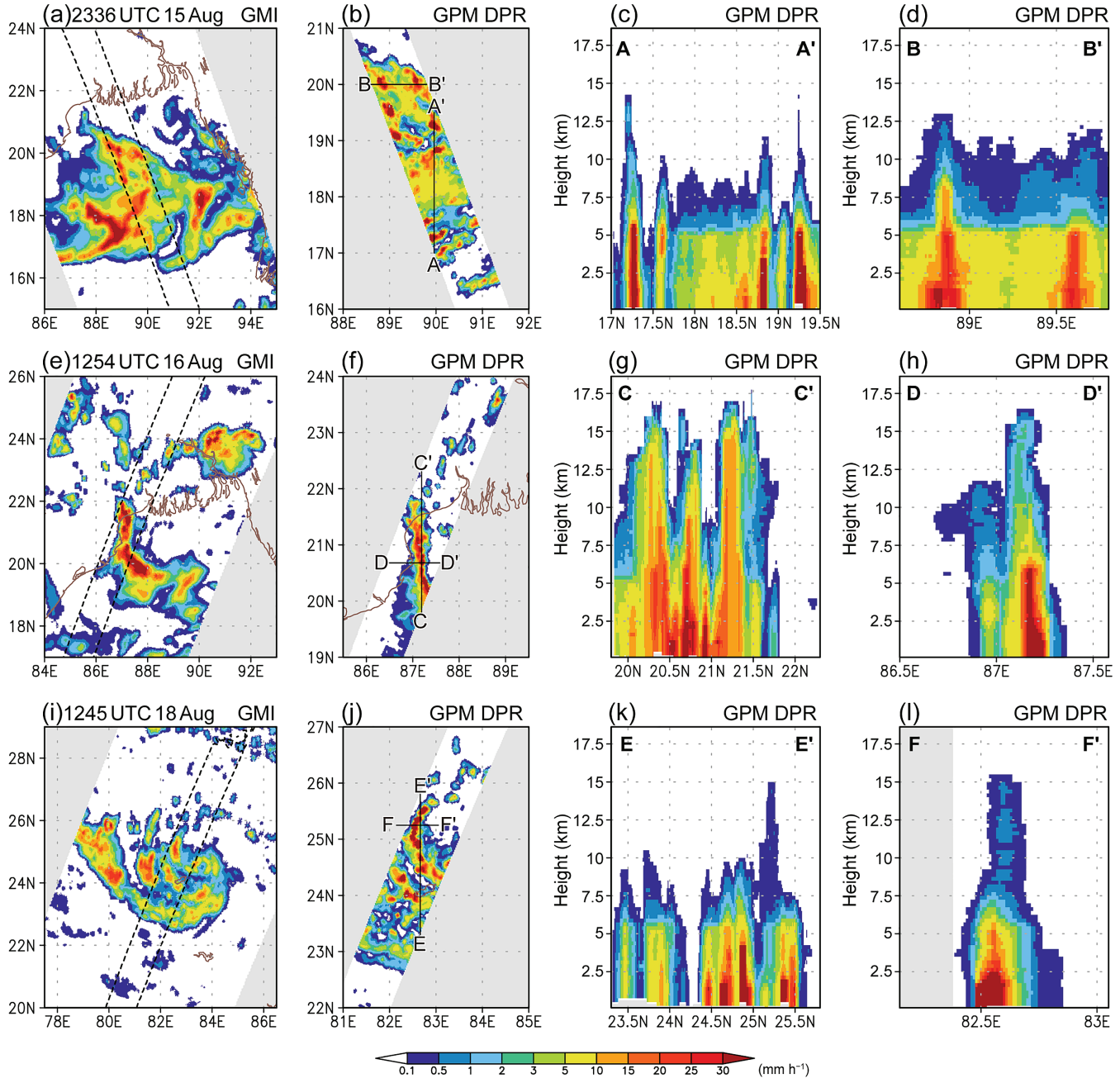


**FIGURE 4** (a) Spatial distribution of precipitation (shading, mm·h$^{-1}$) derived from the GMI at 2336 UTC 15 August 2016; this is an enlarged view of Figure 3e around the target precipitation systems. The area enclosed by grey shading (dashed lines) indicates the GMI (GPM DPR) swath. (b) Spatial distribution of precipitation (shading, mm·h$^{-1}$) at 1,000 m above sea level from GPM DPR. The area enclosed by grey shading indicates the GPM DPR swath. (c) Vertical–latitude section of precipitation (shading, mm·h$^{-1}$) along line A–A' from GPM DPR. (d) Vertical–longitude section along line B–B'. (e,f) As in (a,b), but for 1254 UTC 16 August. (g,h) As in (c,d), but for line C–C' and line D–D'. (i,j) As in (a,b) but for 1245 UTC 18 August. (k,l) As in (c,d), but for 1245 UTC 18 August. The observation times in (a,e,i) correspond to those in Figure 3e,f,h for GMI, respectively [Colour figure can be viewed at wileyonlinelibrary.com].

the low (21°N, 90°E). Some MCSs are observed over northern India in front of the Himalayas where there is convergence between the monsoon westerlies and the easterlies of the monsoon depression (Figure 3b). On 17 August the vortical low develops into the monsoon depression (Figure 1).

The monsoon depression makes landfall at 1200 UTC 17 August and then moves northwestward (not shown). At 0000 UTC 18 August (Figure 3c), active convection is no longer observed over the BoB. Active convection only appears within the monsoon depression and the area of convergence extending northwestward from the monsoon depression over land. Mesoscale spiral rain bands are observed within the monsoon depression after landfall (Figure 3g,h).

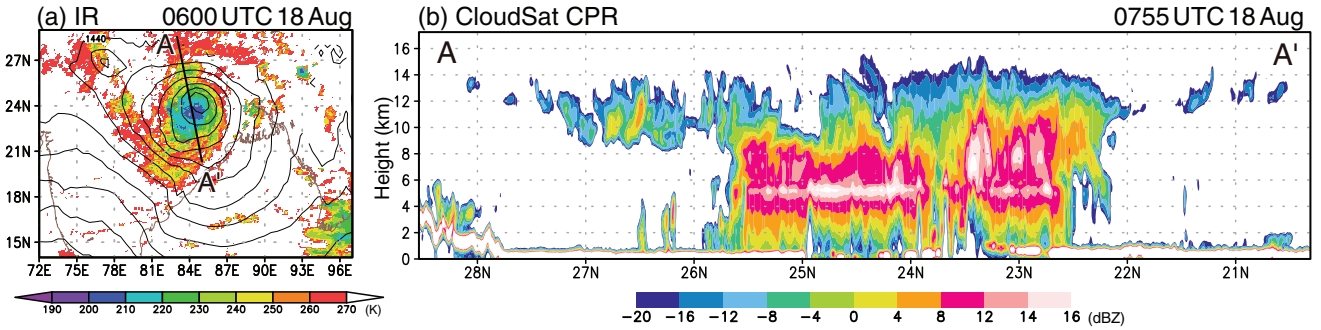


**FIGURE 5** (a) Distribution of infrared brightness temperature (shading, K) from GridSat data and 850 hPa geopotential height from the NCEP CFSv2 at 0600 UTC 18 August 2016. The contour interval for geopotential height is 15 gpm. Line A–A' indicates the CloudSat overpass at 0755 UTC 16 August 2016. (b) Radar reflectivity (dBZ) from CloudSat Cloud Profiling Radar (CPR) along line A–A' [Colour figure can be viewed at wileyonlinelibrary.com].

Figure 4 shows the horizontal distribution and vertical cross-section of precipitation from the DPR for the same dates and times as in Figure 3 except for 2325 UTC 17 August. Note that the radar swaths of DPR only overlap the central portions of the GMI swaths, as shown by the area within the dashed lines in Figure 4a,e,i. At 2336 UTC 15 August (Figure 4a,b), the precipitation area over the BoB consists of a mixture of vertical convective cells and stratiform rainfall with the melting layer at a height of about 5 km (Figure 4c,d), thereby showing the features of MCSs (Maddox, 1980; Houze *et al.*, 2007). Some convective cells exceed 10 km in height; most of the high precipitation signals (>20 mm·h$^{-1}$) are confined below 7 km. At 1254 UTC 16 August (Figure 4e,f), the area of high precipitation around 21°N, 87°E, which is part of the ring-like rain band, consists of a row of vertically upright intense convective cells that exceed 15 km in height (Figure 4g). At 1245 UTC 18 August (Figure 4i), the DPR also detects the finer spiral structure of high precipitation (>20 mm·h$^{-1}$) (Figure 4j). Almost all the precipitation cells along the rain bands have a vertically erect convective structure (Figure 4k), but they are not as high (<10 km) as those on 16 August (Figure 4g).

The CloudSat overpass reveals the inner structure beneath the cloud tops of the monsoon depression at approximately 0755 UTC 18 August (Figure 5). Dense clouds make up the monsoon depression as a whole. The mean cloud top height is around 14 km. The layer with horizontally elongated high reflectivity around 5 km is a melting layer. There is an area of weak reflectivity (i.e. an eye-like structure) between 23.5°N and 24°N, close to the depression centre under high-altitude clouds. The southern portion of the monsoon depression tends to have vertically upright convective echoes (pink colour), whereas a horizontally elongated melting layer without deep upright echoes exists in the northern portion.

## 3.2 | Model experiments

Section 3.1 revealed different features of mesoscale precipitation systems such as the MCS structure with active deep convection cells and stratiform precipitation around 0000 UTC 16 August (Figure 3e), the extremely deep convection cells along a ring-like rain band on the southwestern side of the depression around 1200 UTC 16 August (Figure 3f) and the spiral rain bands (Figure 3g,h) of high precipitation after landfall under the synoptic-scale cloud cover (Figure 3a–d). These different features might be associated with different stages in the development of the monsoon depression. In this section, we investigate the mesoscale features of precipitation systems at different life stages of the depression using CReSS. Then, we propose a mechanism for deep convection during the rapid development phase of the depression.

Central pressure from the CNTL run shows a similar temporal evolution to that in CFSv2 throughout the period (Figure 2). The SLP fields are also well reproduced in terms of spatial distribution and temporal evolution (Figure S1). Thus, the CNTL run simulates well the development of the monsoon depression.

Figure 6 shows the spatial distribution of sea-level pressure (SLP) and precipitation from the CNTL run for 16 to 18 August. The UTC values in Figure 6 are not exactly the same as in Figure 3e–h but correspond to almost the same stage in the life cycle. The horizontal distribution of precipitation from the CNTL run captures well the characteristic features seen in Figure 3e–h. At 0000 UTC 16 August, MCSs with some intense precipitation are found in the head of the BoB with a small closed cyclonic circulation. In contrast, the low-pressure centre is obvious at 1100 UTC 16 August at the head of the BoB (Figure 6b). A ring-like rain band of high precipitation occurs away from the centre of the monsoon depression along the closed isobar over the northernmost BoB. At 0000 UTC 18 August the precipitation bands are elongated in the northwestward direction, west of the monsoon depression, and the model also reproduces some rain bands and the ring-like structure of precipitation around the centre of the depression. The depression has west–southwest precipitation maxima with some spiral-like rain bands (Figure 6d).

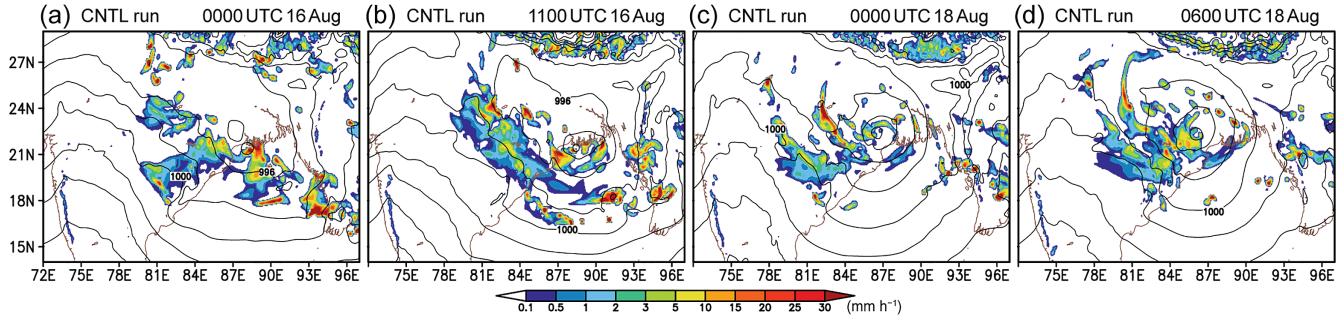


**FIGURE 6** Surface precipitation (shading, mm·h$^{-1}$) and sea-level pressure (contours, hPa) at (a) 0000 UTC 16 August, (b) 1100 UTC 16 August, (c) 0000 UTC 18 August and (d) 0600 UTC 18 August in 2016 simulated by the CNTL run. The contour interval for sea-level pressure is 2 hPa [Colour figure can be viewed at wileyonlinelibrary.com].

Figure 7 presents the vertical structure of the hydrometeors in the CNTL run for the different life stages, as in Figure 6, for comparison with the observed vertical structure from GPM DPR (Figure 4). CReSS does not calculate precipitation intensity as a model output, aside from surface precipitation, but provides vertical distributions of rain, graupel and snow mixing ratios. The vertical distribution of the total mixing ratio of the three hydrometeors corresponds to that of precipitation particles in the precipitation system. The cross-sections are drawn along the meridional and zonal lines that pass over some local maxima of simulated surface precipitation. It is worth noting that the CNTL run successfully simulates the DPR-observed vertical structure of the convective cells. At 0000 UTC 16 August, there is a vertically erect deep convective cell around 21°N and stratiform-like precipitation around 19°N along the line A–A' (Figure 7b), indicative of MCS structure with some convective cells at different development phases. The MCS-like structure is also seen along line B–B'. At 1100 UTC 16 August, convective cells along the ring-like structure, which are located over the northernmost BoB, are deep and intense, and reach 15 km in height along lines C–C' and D–D' around the centre of the low (Figure 7e,f). The deep convective cells have a large amount of graupel, indicative of strong updraught. After landfall of the monsoon depression, the amount of graupel decreases and the heights of precipitation cells generally become lower (Figure 7h,i), consistent with the GPM observations (Figure 4k,l).

An outstanding feature of the precipitation system is extremely deep convection cells around the centre of the low, particularly on the western-to-southwestern side during the rapid developing phase (Figures 4g and 7e). Here, we reveal how deep convection occurs in this area during this phase in the CNTL run. The ring-like distribution of precipitation seen in Figure 7d corresponds to areas of local maxima of low-level moisture flux convergence (Figure 8a). Extremely deep convection is generated at a local maximum of moisture flux convergence along line A–A' in the area where northerlies encounter strong low-level monsoon westerlies on the western side of the low; this is part of a synoptic-scale convergence zone extending northwestward up to the foothills of the Himalayas. A similar feature is found in the observed wind fields (Figures 1 and 3b). The height–latitude cross-section along line A–A' shows that low-level northerlies encounter a thick layer of low-level westerlies around 21.2°N (Figure 8c). The spatial distribution of equivalent potential temperature ($\theta_e$) shows that low-level monsoon westerlies from the Indian subcontinent to the south of 21°N bring relatively dry air (i.e. lower $\theta_e$) toward the head of the BoB (Figure 8b). $\theta_e$ gradually increases moving eastward between 19°N and 21°N. Note that low-level warm, humid air of high $\theta_e$ extends to the north of the centre of the low within a closed cyclonic circulation. Convective available potential energy (CAPE), which is related to the potential updraught strength, is also large (>1,500 J·kg$^{-1}$) in the same region. Surface-based CAPE was used in this study. Hunt *et al.* (2016a) revealed large CAPE and small convective inhibition (CIN) within the monsoon depression from composite monsoon depressions. Air with high $\theta_e$ is confined to below 900 hPa (i.e. the atmospheric boundary layer) to the north of 21.2°N, whereas dry air is found around 700 hPa, resulting in a high degree of conditional instability with large CAPE (Figure 8d). In the area of low-level convergence between northerlies and strong westerlies, the environmental air can be raised up to the level of free convection (LFC), which leads to deep convection due to the release of large CAPE to the west–southwest of the centre of the low. The same mechanism is also applicable to the deep convection at 0000 UTC 16 August shown in Figure 7b. The height–longitude cross-section along line B–B' crosses the centre of the low (Figure 8e), which is located around 88.4°E. The updraught near the centre of the low is caused by the same mechanism as that along line A–A' in Figure 8c. The centre of the low is characterized by high $\theta_e$ from the surface to the mid-troposphere.

As seen in Figures 1 and 3, the monsoon depression develops over the head of the BoB. This means that evaporation from the BoB might be important for cyclogenesis. In fact, the increase of $\theta_e$ toward the leeside in the boundary layer

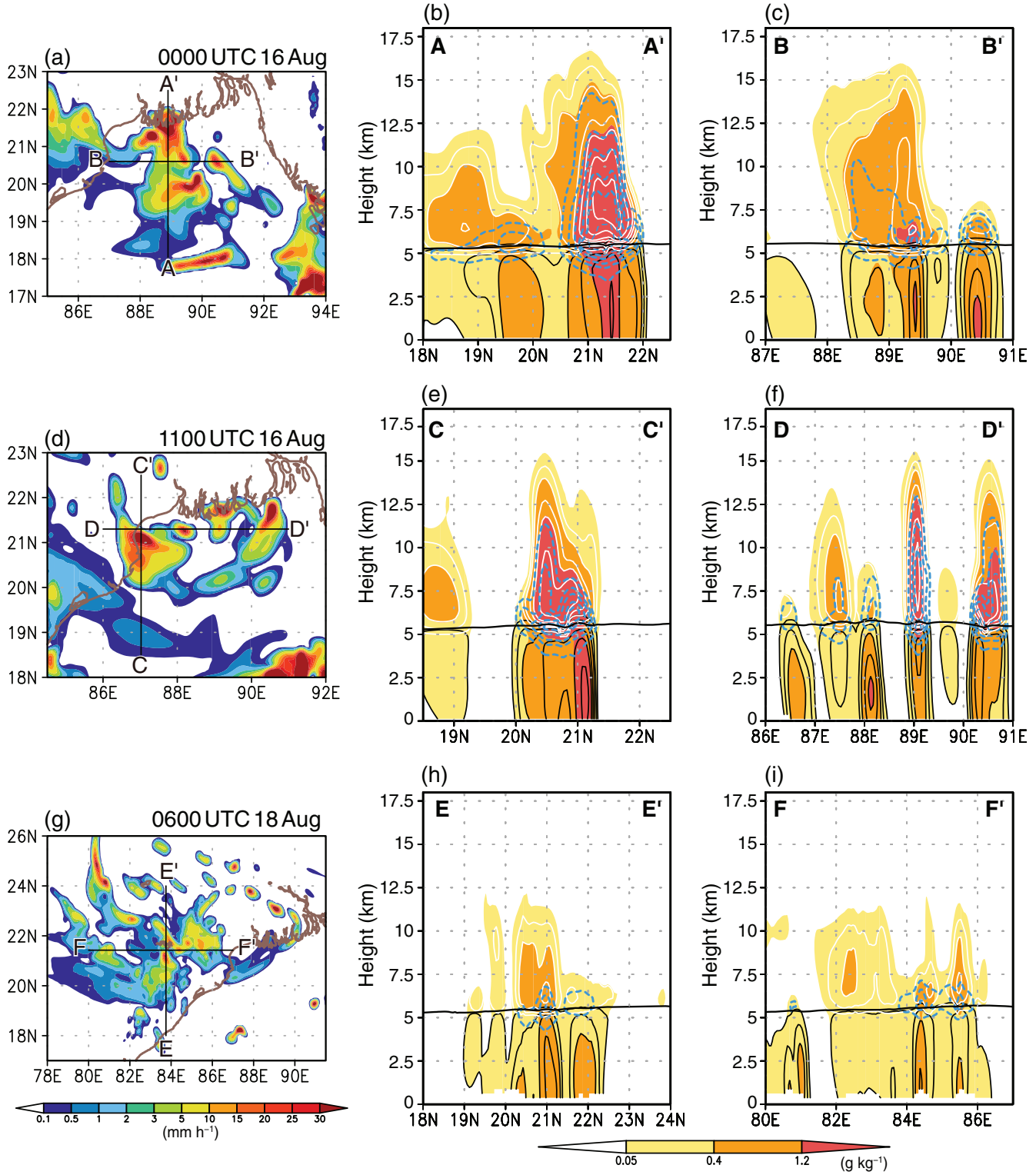


**FIGURE 7** (a) Surface precipitation at 0000 UTC 16 August 2016 simulated by the CNTL run; this is an enlarged view of Figure 6a around the head of the Bay of Bengal. (b,c) Vertical cross-sections of simulated precipitating hydrometeors: rain (black solid contours, g·kg$^{-1}$), graupel (blue dashed contours, g·kg$^{-1}$) and snow (white solid contours, g·kg$^{-1}$) along line A–A' and line B–B', respectively. Shading denotes areas where the sum of the rain, graupel and snow mixing ratios exceeds 0.05 g·kg$^{-1}$, indicating the existence of precipitating particles. The contours for hydrometeor mixing ratios are drawn at 0.05, 0.2, 0.4, 0.8, 1.2, 2.0 and 3.0 g·kg$^{-1}$. The thick solid contour shows the 0 °C level. (d–f) As in (a–c), but for 1100 UTC 16 August when the ring structure of precipitation was observed near the northern coast of the BoB in Figure 6b. Vertical cross-sections are for line C–C' and line D–D'. (g–i) As in (a–c), but for 0600 UTC 18 August after the monsoon depression makes landfall. Vertical sections are for lines E–E' and F–F', respectively [Colour figure can be viewed at wileyonlinelibrary.com].

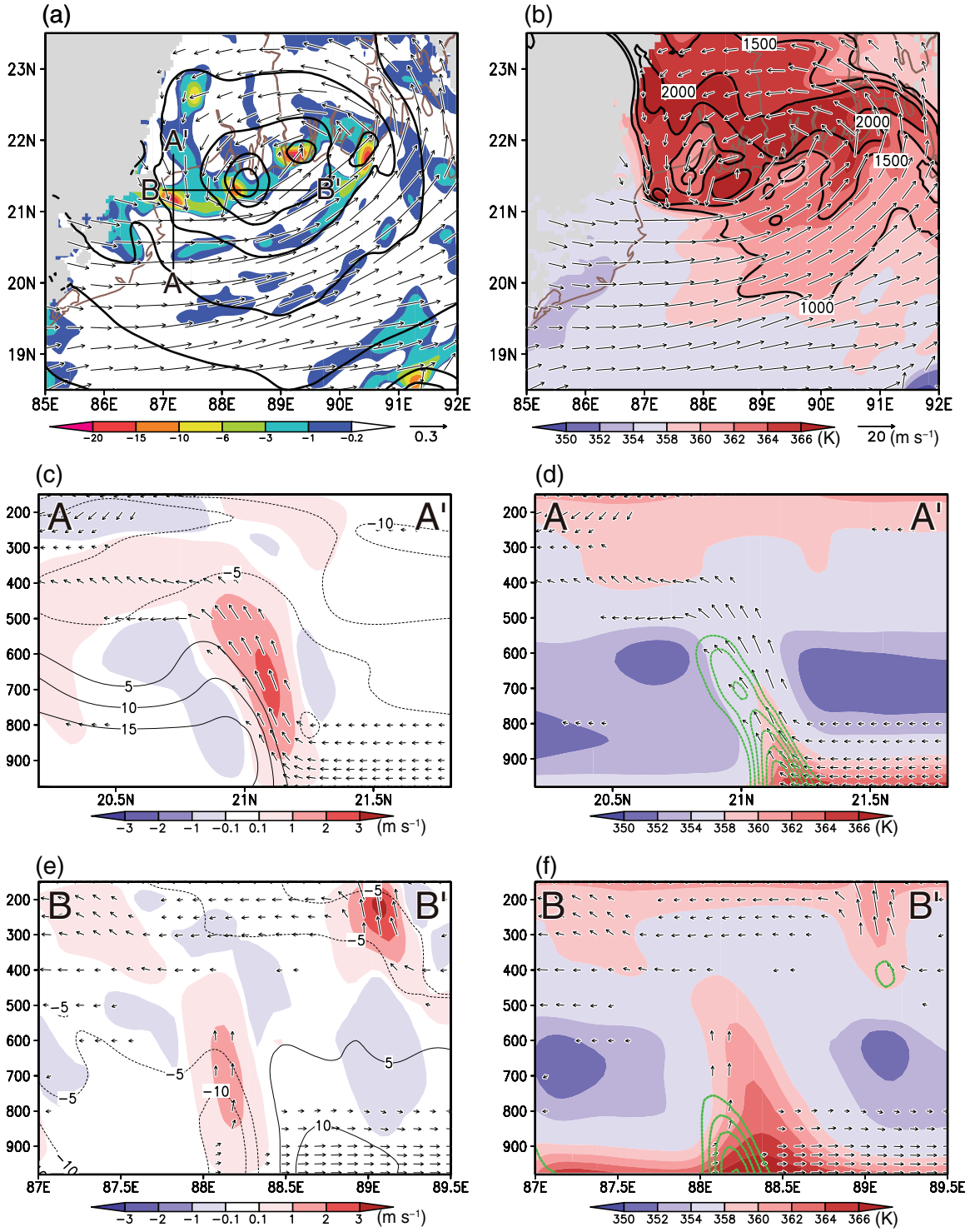


**FIGURE 8** (a) Geopotential height (contours, gpm), water vapour flux (vectors, $kg \cdot kg^{-1} \cdot m \cdot s^{-1}$) and its divergence (shading, $1.0 \times 10^{-6}$ $kg \cdot kg^{-1} \cdot s^{-1}$) at 975 hPa at 1100 UTC 16 August simulated by the CNTL run. The contour interval for geopotential height is 10 gpm. (b) As in (a), but for horizontal wind fields (vectors), equivalent potential temperature (shading, K) and CAPE (contours, $J\,kg^{-1}$). The contour interval of CAPE is $500\,J \cdot kg^{-1}$; contours with values of $<1{,}000\,J \cdot kg^{-1}$ are omitted. (c) Height–latitude cross-section of vertical velocity (shading, $m \cdot s^{-1}$), zonal wind component (contours, $m \cdot s^{-1}$), and meridional and vertical winds (vectors; vertical wind is multiplied by 10) along line A–A' in (a). Only vectors that exceed 1 $m \cdot s^{-1}$ in vertical velocity or 5 $m \cdot s^{-1}$ in meridional wind are plotted. The contour interval for zonal wind is 5 $m \cdot s^{-1}$. (d) As in (c), but for equivalent potential temperature (shading, K) and horizontal water vapour flux divergence (contours, $kg \cdot kg^{-1} \cdot s^{-1}$). Only contours with values less than $-3.0 \times 10^{-6}$ $kg \cdot kg^{-1} \cdot s^{-1}$ are plotted. (e) As in (c), but for the height–longitude cross-section of the meridional wind component (contours) and the zonal and vertical winds (vectors) along line B–B' in (a). (f) As in (e), but for equivalent potential temperature (shading, K) and horizontal water-vapour flux divergence (contours, $kg \cdot kg^{-1} \cdot s^{-1}$) [Colour figure can be viewed at wileyonlinelibrary.com].

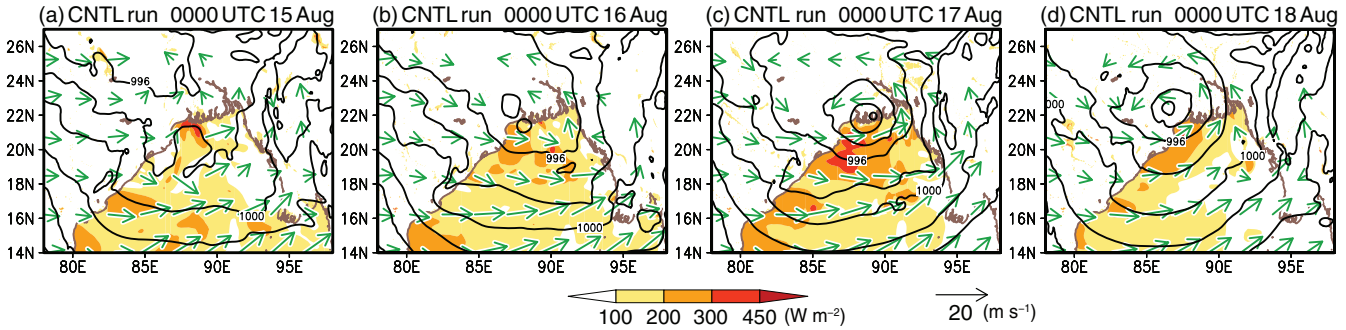


**FIGURE 9** Spatial distribution of sea-level pressure (contours, hPa), 10 m horizontal wind (vectors) and surface latent-heat flux (shading, $W \cdot m^{-2}$) from the CNTL run at 0000 UTC on (a) 15 August, (b) 16 August, (c) 17 August and (d) 18 August 2016. Contour interval for sea-level pressure is 2 hPa. Wind vectors with wind speed less than 3 $m \cdot s^{-1}$ are omitted. Latent-heat flux less than $100 W \cdot m^{-2}$ is omitted [Colour figure can be viewed at wileyonlinelibrary.com].

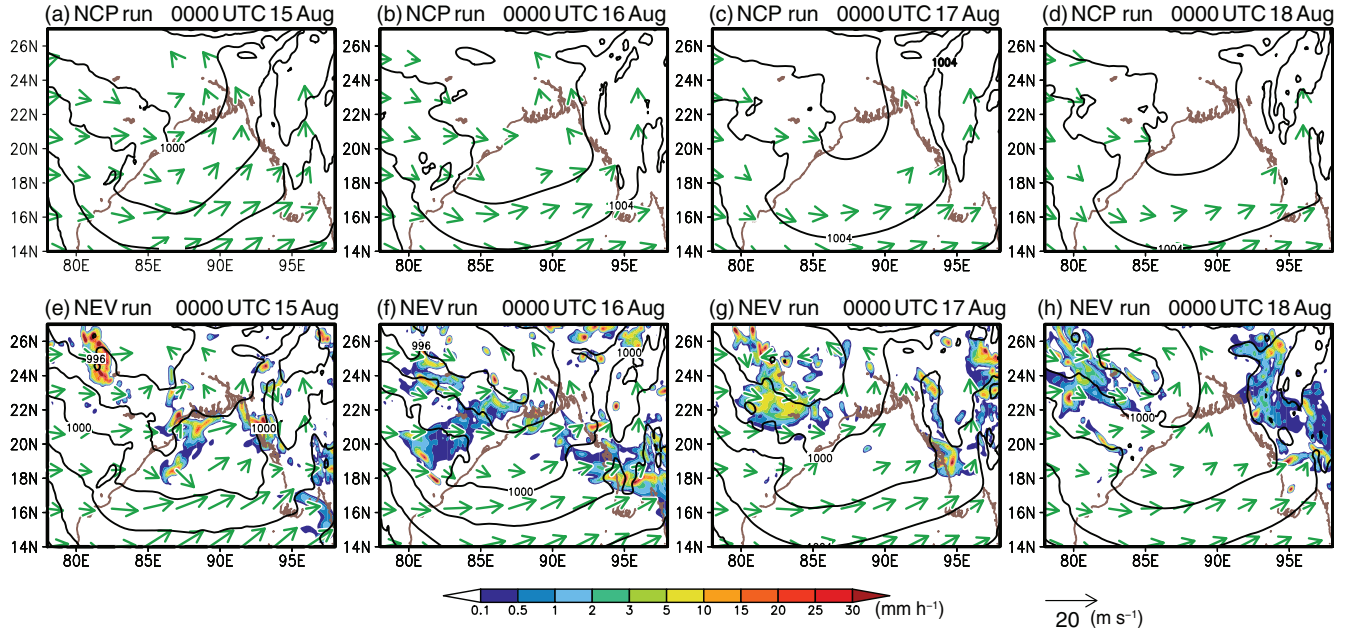


**FIGURE 10** Spatial distribution of sea-level pressure (contours, hPa) and 10 m wind (vectors) at 0000 UTC on (a) 15 August, (b) 16 August, (c) 17 August and (d) 18 August 2016 from the NCP run. Contour interval for sea-level pressure is 2 hPa. Wind vectors with wind speed less than 3 $m \cdot s^{-1}$ are omitted. (e–h) As in (a–d), but for the NEV run. Shading denotes precipitation [Colour figure can be viewed at wileyonlinelibrary.com].

suggests the intake of moisture from the ocean surface to the flowing air (Figure 8b). Figure 9 shows the time sequence of surface latent-heat flux in the CNTL run. At 0000 UTC 15 August (Figure 9a), surface latent-heat flux is large over the southern BoB south of 17°N. From 16 to 17 August (Figure 9b,c), latent-heat flux increases greatly over the head of the BoB as surface wind is enhanced due to the development of the monsoon depression. In addition, the area of high latent-heat flux around 20°N, 87°E corresponds to that of high SST (>29 °C) during 14–16 August according to the daily OI SST dataset (not shown).

To evaluate the respective effects of latent heating of condensation due to cloud/precipitation processes and evaporation from the BoB on the genesis and development of the monsoon depression, we performed two sensitivity experiments: the NCP run and the NEV run. In the NCP run, cloud microphysical processes are not employed during the simulation. Latent heating from condensation does not occur in this run. In the NCP run (Figure 10a–d), unlike the CNTL run (Figure 8e–h), the low does not develop at all around the BoB. The NCP run revealed that latent heat of condensation from active convection (Figures 1,3 and 4) is essential to the development of the monsoon depression, similar to other tropical disturbances such as typhoons and cyclones.

In the NEV run, cloud microphysical processes are active, but evaporation from the BoB is eliminated. At 0000 UTC 15 August (Figure 10e), the spatial distribution of precipitation and SLP is quite similar to that in the CNTL run (Figure 8e). After that, however, SLP does not decrease over the head of the BoB from 16 to 17 August (Figure 10f,g). In addition,

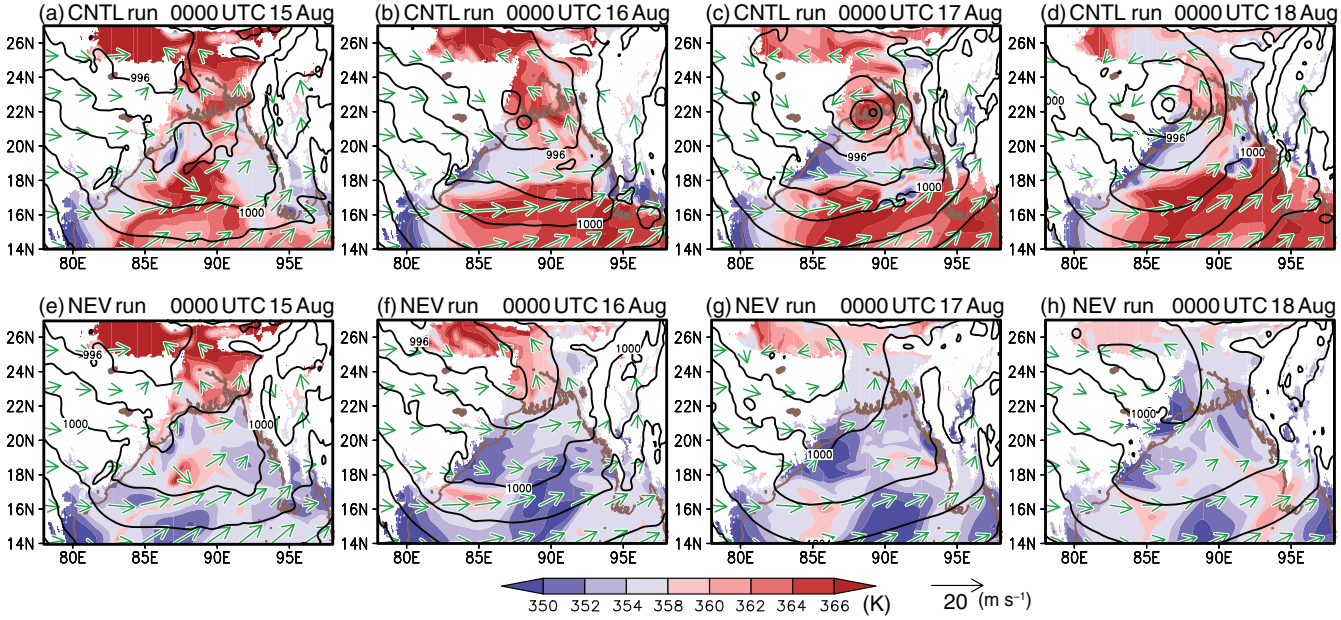


**FIGURE 11** Spatial distribution of sea-level pressure (contours, hPa), 10 m horizontal wind (vectors) and equivalent potential temperature at 975 hPa (shading, K) at 0000 UTC on (a) 15 August, (b) 16 August, (c) 17 August and (d) 18 August 2016 from the CNTL run. White shading indicates areas above 975 hPa (~200 m above sea level). The contour interval for sea-level pressure is 2 hPa. Wind vectors with wind speeds of $<3$ m·s$^{-1}$ are omitted. (e–h) As in (a–d), but for the NEV run [Colour figure can be viewed at wileyonlinelibrary.com].

the vortex core and surrounding precipitation systems do not appear over the head of the BoB. A comparison between the CNTL run and the NEV run demonstrates that the moisture supply from the warm ocean surface over the BoB plays an active role in the rapid intensification of the vortex core over the head of the BoB.

We further investigate how the moisture supply from the BoB provides a suitable environment for rapid development. Figure 11 shows a time sequence of $\theta_e$ in the atmospheric boundary layer for the CNTL and NEV runs. In the CNTL run, at 0000 UTC 15 August (Figure 11a), an area of high $\theta_e$ extends broadly over the BoB, whereas a low-$\theta_e$ area (i.e. a dry area) is observed along the eastern coast of India, leeward of the Indian subcontinent, which contains plateaus and mountains, relative to the low-level monsoon westerlies. During the rapid developing phase of the depression from 16 to 17 August (Figure 11b,c), dry air of low $\theta_e$ extends eastward between 18°N and 19.5°N over the head of the BoB as the low develops, because of the enhanced westerlies blowing from land. In contrast, the low/monsoon depression around the northernmost part of the BoB contains air of high $\theta_e$. The wind field during this phase is similar to that at 1100 UTC 16 August (Figure 8b). After landfall, the high-$\theta_e$ area almost disappears from the northernmost part of the BoB. The NEV run revealed that an air mass of high $\theta_e$ does not form over the BoB without evaporation from the BoB (Figure 11e–h). This influence extends up to the Gangetic Plain. The difference between the CNTL and NEV runs suggests that surface latent-heat flux from the BoB plays a role in maintaining warm, humid air in the boundary layer around the depression during the development phase.

Areas of high $\theta_e$ in the boundary layer correspond to those of large CAPE (Figure 12). On 15 August (Figure 12a), a moderate–large CAPE area extends sporadically over the head of the BoB. From 16 to 17 August (Figure 12b,c), the large-CAPE area extends throughout the low-pressure area near the northernmost part of the BoB. The observational evidence and results from model experiments suggest that deep convection is produced by the release of the instability within the air rising in the area of low-level convergence during the rapid development phase of the monsoon depression. After landfall, the large-CAPE area does not follow the depression (Figure 12d). The CAPE value is small over and around the depression over land. Therefore, the height of the convection cells decreases after landfall (Figure 7g–i). In the NEV run (Figure 12e–h), the lack of evaporation from the BoB leads to a small-CAPE environment over the BoB and the Gangetic Plain, resulting in precipitating convection being suppressed over the BoB.

## 4 | DISCUSSION

### 4.1 | Deep convection, MCSs and a possible feedback

MCSs with embedded deep convection appear near the low, particularly along the western–southwestern side during the rapid development phase of the monsoon depression over the

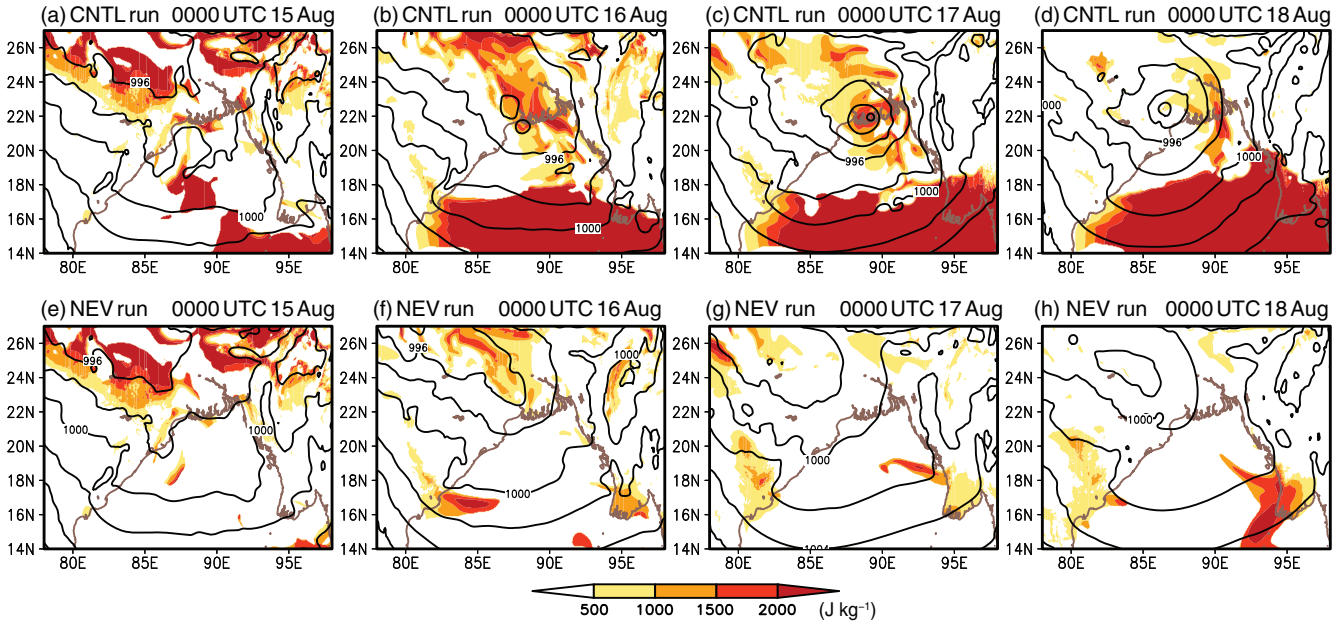


**FIGURE 12** Spatial distribution of sea-level pressure (contours, hPa) and CAPE (shading, J·kg$^{-1}$) at 0000 UTC on (a) 15 August, (b) 16 August, (c) 17 August, and (d) 18 August 2016 from the CNTL run. The contour interval for sea-level pressure is 2 hPa. (e–h) As in (a–d), but for the NEV run [Colour figure can be viewed at wileyonlinelibrary.com].

head of the BoB (Figures 4a–h and 7a–f). The large CAPE environment and release of the instability over the area of low-level convergence probably generate MCSs with embedded deep convection (Figure 8a,b). Evaporation from the head of the BoB maintains the humid boundary layer within the low during this phase. The maxima of surface latent-heat flux correspond to areas of strong dry air inflow from the Indian subcontinent to the south of the low (Figures 9b,c and 11b,c) and SST maxima along the western coast of the head of the BoB. These conditions might enhance evaporation from the head of the BoB and add a large amount of moisture to the air flowing inward toward the low/monsoon depression (Figure 8b).

The southwesterlies/southerlies on the eastern side of the low draw in warm humid boundary-layer air to the low, maintaining a large-CAPE environment and refuelling the deep convection. Then, the warm humid air enters the boundary layer in the closed cyclonic circulation of the low near the northernmost part of the BoB. Despite the large-CAPE environment, moist convection is supressed in the northern-to-northeastern part of the low/monsoon depression (Figures 1 and 6b). In fact, weak subsidence appears in the mid- to upper-level troposphere in the CNTL run (figure not shown). Synoptic-scale weak subsidence was observed in monsoon depressions to the north–northeast of the low/-monsoon depression (Fujinami *et al.*, 2017). Weak subsidence might result in the dry air (i.e. low $\theta_e$) around 600–700 hPa to the north of 21°N (Figure 8d), resulting in the high degree of conditional instability. Then, moist boundary-layer air is transported southward by northerlies/northeasterlies that make up the western part of the closed cyclonic circulation of the low, without a large consumption of water vapour because of the supressed moist convection. The moist low-level northerlies eventually encounter strong westerlies on the western and southwestern sides of the low. The low-level air is raised up to the LFC and large CAPE is released, resulting in the generation of extremely deep convection and MCSs.

Isolated deep convection and MCSs exist within the developing tropical depression/cyclone, similar to the monsoon depression. In tropical depressions/cyclones, Houze (2010) illustrated conceptually that the vorticity of the low-level environment is stretched by convergence related to deep convection at the base of convective updraughts and is advected upward. These updraughts result in centres of high positive vorticity being extended upward. An MCS begins as one or more such isolated instances of deep convection. The MCS has both a convective and a stratiform component during its mature stage. The stratiform region of the MCS also accumulates positive vorticity from the remaining portions of the convective cells to form a mid-level mesoscale convective vortex. The low as a whole develops rapidly through such processes related to the MCS life cycle. Murthy and Boos (2019) also demonstrated that heating from both deep convection and stratiform precipitation systems can produce the observed vertical distribution of potential vorticity in tropical depressions, indicating the development of tropical depressions through the generation of positive potential vorticity from the heating. Our study revealed that deep convection cells and stratiform precipitation are indeed observed within the low in the rapid development phase of the monsoon depression. Thus, the

development processes of tropical depressions proposed by the previous studies may be applicable to monsoon depressions, although further detailed study is needed to clarify the respective effects of deep convective and stratiform rain systems embedded in the MCS on the rapid development of the monsoon depressions.

Further intensification of the low due to the development of deep convection and MCSs enhances the wind speed around the low and, in turn, might promote more evaporation from the BoB and moist air inflow into the low/monsoon depression, leading to larger CAPE and more intense moist convection. This positive feedback might lead to the rapid intensification of the monsoon depression over the head of the BoB.

### 4.2 | Genesis environment for monsoon depressions

Recent studies have proposed that barotropic instability can explain the structure, propagation and geographic distribution of monsoon depressions (Mishra, 2018; Diaz and Boos, 2019). Intraseasonal oscillations such as the BSISO and QBW change the location of the strong meridional cyclonic shear zone over the BoB that strongly controls the genesis locations and tracks of the depressions (Goswami *et al.*, 2003; Hatsuzuka and Fujinami, 2017). When the low-level monsoon westerlies are enhanced and the core of the westerlies appears around ∼15°N over the BoB due to the propagation of the BSISO and QBW, LPSs including monsoon depressions occur frequently over the head of the BoB (Hatsuzuka and Fujinami, 2017). The monsoon depression of the present study occurred under an atmospheric environment suitable for cyclogenesis in low-level wind fields, similar to that shown by Hatsuzuka and Fujinami (2017) (Figure 1). The strong meridional cyclonic shear zone of monsoon westerlies around the monsoon trough can be a favourable environment for barotropic instability. However, it cannot explain the rapid growth of the monsoon depression over the BoB (Diaz and Boos, 2019). The atmospheric environment and condensational heating from the convection cells might jointly promote the growth of monsoon depressions over the BoB. Observed monsoon depressions tend to retain their strength in a few days after landfall without a rapid decline, unlike a typhoon. In fact, the monsoon depression in this study keeps its strength and vortical structure from 1800 UTC 17 August to 0000 UTC 20 August, after landfall (Figure 2). Barotropic instability might explain why the monsoon depression can persist after landfall in conjunction with condensation heating from convection. The detailed mechanism of the genesis of low-pressure systems remains unclear, although latent heating is a major driver of their development. Monsoon depressions often develop from the re-genesis of westward-propagating residual lows, which include tropical depressions and lows related to QBW, from the South China Sea across the Indochina Peninsula (Chen and Weng, 1999). How the initial vortex is generated in an environment of rich cyclonic vorticity related to the monsoon trough is also an important problem for future work.

## 5 | SUMMARY

We have investigated the hydrometeors of the monsoon depression that occurred on 17 August 2016 over the Bay of Bengal (BoB) using infrared brightness temperature, GPM GMI, GPM DPR and CloudSat CPR data in the different stages of the monsoon depression life cycle, focusing on the mesoscale precipitation systems. In the rapid development stage of the low from 0000 to 1200 UTC on 16 August, a day before the depression reached monsoon depression intensity, active convection with an MCS structure is observed over the northernmost BoB. A ring-like rain band with very deep convective cells appears at a radial distance of a few hundred kilometres from the centre of the depression, as the vortical low structure becomes evident. The lowest central pressure is observed at 0000 UTC 17 August and the low becomes a monsoon depression over the northernmost BoB. Intense convection occurs in the south–southwest region of the monsoon depression, which is typical of monsoon depressions. After reaching minimum central pressure over the northernmost BoB, the monsoon depression moves northwestward and makes landfall at 1200 UTC 17 August. After landfall, the central pressure of the depression increases gradually. The monsoon depression has mesoscale spiral rain bands. The height of precipitation cells in the rain bands becomes lower than in the developing stage over the BoB. Dense clouds cover the monsoon depression with taller convective clouds in its southern part.

We used the CReSS non-hydrostatic and compressible cloud-resolving model to investigate the time variation of hydrometeors observed by satellites and a mechanism for deep convection in the rapid development phase of monsoon depressions. CReSS performed reasonably well in reproducing the observed spatio-temporal variation of the monsoon depression from the development stage over the BoB through the decaying phase after landfall. Features of the mesoscale structure of precipitation, such as active convection cells with an MCS structure over the northernmost BoB and a subsequent ring-like rain band with deep convective cells, are also well reproduced. The deep convective cells appear in the western-to-southwestern part of the low during the rapid development phase of the monsoon depression. The deep convective cells are generated by the release of large CAPE in the area of low-level convergence between northerlies with large-CAPE air mass, which make up the western part of a closed cyclonic circulation centred on the northernmost part of the BoB, and monsoon westerlies with relatively dry air mass to the south of the cyclonic circulation.

Two sensitivity experiments were performed to evaluate the effects of latent heating from cloud/precipitation processes and evaporation from the BoB on the development of the monsoon depression. The NCP (i.e. no cloud microphysics processes) run could not reproduce the development of the low throughout the simulation. Thus, latent heating due to condensation from active convection is essential for the growth of the monsoon depression, similar to tropical disturbances such as typhoons and cyclones. The effect of latent-heat supply from the BoB is evident from the comparison between the CNTL and NEV (i.e. no evaporation from the BoB) runs. Evaporation from the BoB adds a large amount of moisture to the atmospheric boundary layer near the low over the head of the BoB. The southwesterlies/-southerlies on the eastern side of the low draw in warm, humid boundary-layer air to the closed cyclonic circulation of the low, maintaining a large-CAPE environment in the low around the head of the BoB. Northerlies with large-CAPE air mass encounter strong westerlies in the western/southwestern part of the low, resulting in deep convective cells driven by the instability. Without evaporation from the BoB, deep convection cannot develop around the BoB because of the small-CAPE environment. Thus, both cloud/precipitation processes and evaporation from the BoB are essential for the rapid growth of the monsoon depression over the head of the BoB.

Although this study examined only one typical monsoon depression, it reveals some novel findings about the mesoscale structure of cloud/precipitation systems in a monsoon depression during the different stages of its life cycle. To fully understand the common mesoscale features of cloud/-precipitation in monsoon depressions, further studies are needed of multiple monsoon depressions based on a ground precipitation radar network that can observe the whole life cycle of the depression with high spatio-temporal resolution.

Our results demonstrate that latent heating from the BoB is important for the development of monsoon depressions. Most monsoon depressions over the BoB are generated to the north of 15°N (e.g. Hatsuzuka *et al.*, 2014; Hunt *et al.*, 2016a), but the genesis location varies from coastal to offshore areas. More monsoon depressions should be examined in the future to reveal other processes related to ocean–atmosphere interactions during the rapid development phase.

## ACKNOWLEDGEMENTS

We thank Nobuhiro Takahashi, Hirohiko Masunaga and Hironari Kanamori for their valuable comments and suggestions. We also thank two anonymous reviewers for helping to improve the manuscript. This study was conducted with support from the Japan Society for the Promotion of Science (JSPS) KAKENHI Grants JP 26220202, JP 26400465 and JP 18KK0098. Parts of this study were conducted under a collaborative research programme of the Institute for Space-Earth Environmental Research, Nagoya University.

## ORCID

*Hatsuki Fujinami* https://orcid.org/0000-0002-2400-479X
*Hidetaka Hirata* https://orcid.org/0000-0001-6078-9101

## REFERENCES

Akter, N. and Tsuboki, K. (2012) Numerical simulation of cyclone *Sidr* using a cloud-resolving model: characteristics and formation process of an outer rainband. *Monthly Weather Review*, 140, 789–810.

Baisya, H., Pattnaik, S. and Rajesh, P.V. (2017) Land surface–precipitation feedback analysis for a landfalling monsoon depression in the Indian region. *Journal of Advances in Modeling Earth Systems*, 9, 712–726. https://doi.org/10.1002/2016MS000829.

Berry, G.J., Reeder, M.J. and Jakob, C. (2012) Coherent synoptic disturbances in the Australian monsoon. *Journal of Climate*, 25, 8409–8421. https://doi.org/10.1175/jcli-d-12-00143.1.

Bohlinger, P., Sorteberg, A. and Sodemann, H. (2017) Synoptic conditions and moisture sources actuating extreme precipitation in Nepal. *Journal of Geophysical Research-Atmospheres*, 122, 12653–12671. https://doi.org/10.1002/2017JD027543.

Chang, H.-I., Niyogi, D., Kumar, A., Kishtawal, C.M., Dudhia, J., Chen, F., Mohanty, U.C. and Shepherd, M. (2009) Possible relation between land surface feedback and the post-landfall structure of monsoon depressions. *Geophysical Research Letters*, 36, L15826. https://doi.org/10.1029/2009GL037781.

Chattergee, P. and Goswami, B.N. (2004) Structure, genesis and scale selection of the tropical quasi-biweekly mode. *Quarterly Journal of Royal Meteorological Society*, 130, 1171–1194.

Chen, T. and Weng, S. (1999) Interannual and intraseasonal variations in monsoon depressions and their westward-propagating predecessors. *Monthly Weather Review*, 127, 1005–1020.

Cohen, N.Y. and Boos, W.R. (2016) Perspectives on moist baroclinic instability: implications for the growth of monsoon depressions. *Journal of the Atmospheric Sciences*, 73, 1767–1788.

Deardorff, J.W. (1980) Stratocumulus-capped mixed layers derived from a three dimensional model. *Boundary-Layer Meteorology*, 18, 497–527.

Diaz, M. and Boos, W.R. (2019) Barotropic growth of monsoon depressions. *Quarterly Journal of the Royal Meteorological Society*, 145(719), 824–844. https://doi.org/10.1002/qj.3467.

Ditchek, S.D., Boos, W.R., Camargo, S.J. and Tippett, M.K. (2016) A genesis index for monsoon disturbances. *Journal of Climate*, 29, 5189–5203.

Dong, W., Lin, Y., Wright, J.S., Ming, Y., Xie, Y., Wang, B., Luo, Y., Huang, W., Huang, J., Wang, L., Tian, L., Peng, Y. and Xu, F. (2016) Summer rainfall over the southwestern Tibetan plateau controlled by deep convection over the Indian subcontinent. *Nature Communications*, 7, 10925. https://doi.org/10.1038/ncomms10925.

Dong, W.H., Lin, Y.L., Wright, J.S., Xie, Y.Y., Xu, F.H., Xu, W.Q. and Wang, Y. (2017) Indian monsoon low-pressure systems feed up-and-over moisture transport to the southwestern Tibetan plateau. *Journal of Geophysical Research: Atmospheres*, 122, 12140–12151. https://doi.org/10.1002/2017JD027296.

Dong, W., Lin, Y., Wright, J.S., Xie, Y., Xu, F., Yang, K., Li, X., Tian, L., Zhao, X. and Cao, D. (2018) Connections between a late summer

snowstorm over the southwestern Tibetan plateau and a concurrent Indian monsoon low-pressure system. *Journal of Geophysical Research: Atmospheres*, 123, 13676–13691. https://doi.org/10.1029/2018JD029710.

Fujinami, H., Yasunari, T. and Motimoto, A. (2014) Dynamics of distinct intraseasonal oscillation in summer monsoon rainfall over the Meghalaya-Bangladesh-western Myanmar region: covariability between the Tropics and mid-latitudes. *Climate Dynamics*, 43, 2147–2166. https://doi.org/10.1007/s00382-013-2040-1.

Fujinami, H., Sato, T., Kanamori, H. and Murata, F. (2017) Contrasting features of monsoon precipitation around the Meghalaya plateau under westerly and easterly regimes. *Journal of Geophysical Research: Atmospheres*, 122, 9591–9610. https://doi.org/10.1002/2016JD026116.

Godbole, R.V. (1977) The composite structure of the monsoon depression. *Tellus*, 29, 25–40. https://doi.org/10.1111/j.2153-3490.1977.tb00706.x.

Goswami, B.N., Ajayamohan, R.S., Xavier, P.K. and Sengupta, D. (2003) Clustering of synoptic activity by Indian summer monsoon intraseasonal oscillations. *Geophysical Research Letters*, 30, 1431. https://doi.org/10.1029/2002GL016734.

Hatsuzuka, D. and Fujinami, H. (2017) Effects of the south Asian monsoon intraseasonal modes on genesis of low pressure systems over Bangladesh. *Journal of Climate*, 30, 2481–2499. https://doi.org/10.1175/Jcli-D-16-0360.1.

Hatsuzuka, D., Yasunari, T. and Fujinami, H. (2014) Characteristics of low pressure systems associated with intraseasonal oscillation of rainfall over Bangladesh during boreal summer. *Monthly Weather Review*, 142, 4758–4774. https://doi.org/10.1175/Mwr-D-13-00307.1.

Hirata, H., Kawamura, R., Kato, M. and Shinoda, T. (2015) Influential role of moisture supply from the Kuroshio/Kuroshio extension in the rapid development of an extratropical cyclone. *Monthly Weather Review*, 143, 4126–4144.

Hirata, H., Kawamura, R., Kato, M. and Shinoda, T. (2016) Response of rapidly developing extratropical cyclones to sea surface temperature variations over the western Kuroshio-Oyashio confluence region. *Journal of Geophysical Research: Atmospheres*, 121, 3843–3858.

Hou, A.Y., Kakar, R.K., Neeck, S., Azarbarzin, A.A., Kummerow, C.D., Kojima, M., Oki, R., Nakamura, K. and Iguchi, T. (2014) The global precipitation measurement mission. *Bulletin of the American Meteorological Society*, 95, 701–722.

Houze, R.A., Jr. (2010) Clouds in tropical cyclones. *Monthly Weather Review*, 138, 293–344. https://doi.org/10.1175/2009MWR2989.1.

Houze, R.A., Jr., Wilton, D.C. and Smull, B.F. (2007) Monsoon convection in the Himalayan region as seen by the TRMM precipitation radar. *Quarterly Journal of the Royal Meteorological Society*, 133, 1389–1411. https://doi.org/10.1002/qj.106.

Houze, R.A., Jr., Rasmussen, K.L., Medina, S., Brodzik, S.R. and Romatschke, U. (2011) Anomalous atmospheric events leading to the summer 2010 floods in Pakistan. *Bulletin of the American Meteorological Society*, 92, 291–298. https://doi.org/10.1175/2010BAMS3173.1.

Hunt, K.M.R. and Fletcher, J.K. (2019) The relationship between Indian monsoon rainfall and low-pressure systems. *Climate Dynamics*, 53, 1859–1871. https://doi.org/10.1007/s00382-019-04744-x.

Hunt, K.M.R., Turner, A.G., Inness, P.M., Parker, D.E. and Levine, R.C. (2016a) On the structure and dynamics of Indian monsoon depressions. *Monthly Weather Review*, 144, 3391–3416.

Hunt, K.M.R., Turner, A.G. and Parker, D.E. (2016b) The spatiotemporal structure of precipitation in Indian monsoon depressions. *Quarterly Journal of the Royal Meteorological Society*, 142(701), 3195–3210. https://doi.org/10.1002/qj.2901.

Hurley, J.V. and Boos, W.R. (2015) A global climatology of monsoon low-pressure systems. *Quarterly Journal of the Royal Meteorological Society*, 141, 1049–1064.

Iguchi, T., Seto, S., Meneghini, R., Yoshida, N., Awaka, J., Le, M., Chandrasekar, V. and Kubota, T. (2015) GPM/DPR level-2. *Algorithm Theoretical Basis Doc*., 68 pp. Available at: http://pps.gsfc.nasa.gov/Documents/ATBD_DPR_2015_whole_a.pdf [Accessed 1st November 2019].

Ikawa, M. and Saito, K. (1991) *Description of a nonhydrostatic model developed at the forecast research department of the MRI*, Technical Reports of the Meteorological Research Institute, 28, 1–283. Available at: http://www.mri-jma.go.jp/Publish/Technical/DATA/VOL_28/28.pdf [Accessed 1st November 2019].

Joseph, S., Sahai, A.K., Sharmila, S., Abhilash, S., Borah, N., Chattopadhyay, R., Pillai, P.A., Rajeevan, M. and Kumar, A. (2015) North Indian heavy rainfall event during June 2013: diagnostics and extended range prediction. *Climate Dynamics*, 44, 2049–2065. https://doi.org/10.1007/s00382-014-2291-5.

Kikuchi, K., Wang, B. and Kajikawa, Y. (2012) Bimodal representation of the tropical intraseasonal oscillation. *Climate Dynamics*, 38, 1989–2000. https://doi.org/10.1007/s00382-011-1159-1.

Knapp, K.R., Ansari, S., Bain, C.L., Bourassa, M.A., Dickinson, M.J., Funk, C., Helms, C.N., Hennon, C.C., Holmes, C.D., Huffman, G.J., Kossin, J.P., Lee, H.T., Loew, A. and Magnusdottir, G. (2011) Globally gridded satellite observations for climate studies. *Bulletin of the American Meteorological Society*, 92, 893–907.

Krishnamurthy, V. and Ajayamohan, R.S. (2010) Composite structure of monsoon low pressure systems and its relation to Indian rainfall. *Journal of Climate*, 23, 4285–4305. https://doi.org/10.1175/2010jcli2953.1.

Krishnamurti, T.N., Martin, A., Krishnamurti, R., Simon, A., Thomas, A. and Kumar, V. (2013) Impacts of enhanced CCN on the organization of convection and recent reduced counts of monsoon depressions. *Climate Dynamics*, 41, 117–134. https://doi.org/10.1007/s00382-012-1638-z.

Lang, T.J. and Barros, A.P. (2002) An investigation of the onsets of the 1999 and 2000 monsoons in central Nepal. *Monthly Weather Review*, 130, 1299–1316. https://doi.org/10.1175/1520-0493(2002)130<1299:Aiotoo>2.0.Co;2.

Maddox, R.A. (1980) Mesoscale convective complexes. *Bulletin of the American Meteorological Society*, 61, 1374–1387.

Mishra, S.K. (2018) On the evolution of planetary-scale fields and genesis of monsoon depressions over the Indian region. *Quarterly Journal of the Royal Meteorological Society*, 144(710), 129–141. https://doi.org/10.1002/qj.3189.

Moorthi, S. and Arakawa, A. (1985) Baroclinic instability with cumulus heating. *Journal of the Atmospheric Sciences*, 42, 2007–2031. https://doi.org/10.1175/1520–0469(1985)042<2007:Biwch>2.0.Co;2.

Murakami, M. (1990) Numerical modeling of dynamical and microphysical evolution of an isolated convective cloud – the 19 July 1981 CCOPE cloud. *Journal of Meteorological Society of Japan. Ser. II*, 68, 107–128. https://doi.org/10.2151/jmsj1965.68.2_107.

Murakami, M., Clark, T.L. and Hall, W.D. (1994) Numerical simulations of convective snow clouds over the Sea of Japan: two-dimensional simulations of mixed layer development and convective snow cloud

formation. *Journal of Meteorological Society of Japan. Series II*, 72, 43–62. https://doi.org/10.2151/jmsj1965.72.1_43.

Murthy, V.S. and Boos, W.R. (2019) Understanding the vertical structure of potential vorticity in tropical depressions. *Quarterly Journal of the Royal Meteorological Society*, 145(722), 1968–1991. https://doi.org/10.1002/qj.3539.

Praveen, V., Sandeep, S. and Ajayamohan, R.S. (2015) On the relationship between mean monsoon precipitation and low pressure systems in climate model simulations. *Journal of Climate*, 28, 5305–5324. https://doi.org/10.1175/JCLI-D-14-00415.1.

Saha, K., Sanders, F. and Shukla, J. (1981) Westward propagating predecessors of monsoon depressions. *Monthly Weather Review*, 109, 330–343.

Saha, S., Moorthi, S., Wu, X., Wang, J., Nadiga, S., Tripp, P., Behringer, D., Hou, Y.T., Chuang, H.Y., Iredell, M., Ek, M., Meng, J., Yang, R., Mendez, M.P., van den Dool, H., Zhang, Q., Wang, W., Chen, M. and Becker, E. (2010) The NCEP climate forecast system reanalysis. *Bulletin of the American Meteorological Society*, 91, 1015–1057. https://doi.org/10.1175/2010bams3001.1.

Samanta, D., Hameed, S.N., Jin, D., Thilakan, V., Ganai, M., Rao, S.A. and Deshpande, M. (2018) Impact of a narrow coastal bay of Bengal Sea surface temperature front on an Indian summer monsoon simulation. *Scientific Reports*, 8, 17694. https://doi.org/10.1038/s41598-018-35735-3.

Sikka, D.R. (1977) Some aspects of the life history, structure and movement of monsoon depressions. *Pure and Applied Geophysics*, 115, 1501–1529. https://doi.org/10.1007/bf00874421.

Stano, G., Krishnamurti, T.N., Kumar, T.S.V.V. and Chakraborty, A. (2002) Hydrometeor structure of a composite monsoon depression using the TRMM radar. *Tellus A*, 54, 370–381.

Tsuboi, A. and Takemi, T. (2014) The interannual relationship between MJO activity and tropical cyclone genesis in the Indian Ocean. *Geoscience Letters*, 1, 9. https://doi.org/10.1186/2196-4092-1-9.

Tsuboki, K. (2008) High-resolution simulations of high-impact weather systems using the cloud-resolving model on the Earth Simulator. In: Hamilton, K. and Ohfuchi, W. (Eds.) *High Resolution Numerical Modeling of the Atmosphere and Ocean*. New York: Springer, pp. 141–156.

Tsuboki, K. and Sakakibara, A. (2002) Large-scale parallel computing of cloud resolving storm simulator. In: Zima, H.P., Joe, K., Sato, M., Seo, Y. and Shimasaki, M. (Eds.) *High Performance Computing. Lecture Notes in Computer Science*, Vol. 2327. Berlin: Springer, pp. 243–259.

Tsuboki, K. and Sakakibara, A. (2007) Numerical prediction of high-impact weather systems – The text book for Seventeenth IHP training course in 2007 (HyARC, Nagoya University, Japan, and UNESCO), 1–273.

Tsuboki, K., Yoshioka, M.K., Shinoda, T., Kato, M., Kanada, S. and Kitoh, A. (2015) Future increase of supertyphoon intensity associated with climate change. *Geophysical Research Letters*, 42, 646–652. https://doi.org/10.1002/2014GL061793.

Ueno, K., Toyotsu, K., Bertolani, L. and Tartari, G. (2008) Stepwise onset of monsoon weather observed in the Nepal Himalaya. *Monthly Weather Review*, 136, 2507–2522. https://doi.org/10.1175/2007mwr2298.1.

Wang, B., Webster, P., Kikuchi, K., Yasunari, T. and Qi, Y.J. (2006) Boreal summer quasi-monthly oscillation in the global Tropics. *Climate Dynamics*, 27, 661–675. https://doi.org/10.1007/s00382-006-0163-3.

Webster, P.J., Toma, V.E. and Kim, H.M. (2011) Were the 2010 Pakistan floods predictable? *Geophysical Research Letters*, 38, L04806. https://doi.org/10.1029/2010GL046346.

Yanase, W., Satoh, M., Taniguchi, H. and Fujinami, H. (2012) Seasonal and intraseasonal modulation of tropical cyclogenesis environment over the Bay of Bengal during the extended summer monsoon. *Journal of Climate*, 25, 2914–2930. https://doi.org/10.1175/Jcli-D-11-00208.1.

Yoon, J.H. and Chen, T.C. (2005) Water vapor budget of the Indian monsoon depression. *Tellus A*, 57, 770–782.

## SUPPORTING INFORMATION

Additional supporting information may be found online in the Supporting Information section at the end of this article.

**How to cite this article:** Fujinami H, Hirata H, Kato M, Tsuboki K. Mesoscale precipitation systems and their role in the rapid development of a monsoon depression over the Bay of Bengal. *Q J R Meteorol Soc*. 2020;146:267–283. https://doi.org/10.1002/qj.3672